An Edge-Referenced Surface Fresh Layer in the Beaufort Sea Seasonal Ice Zone

SARAH R. DEWEY, JAMES H. MORISON, AND JINLUN ZHANG

Polar Science Center, Applied Physics Laboratory, University of Washington, Seattle, Washington

(Manuscript received 7 July 2016, in final form 1 March 2017)

ABSTRACT

To understand the factors causing the interannual variations in the summer retreat of the Beaufort Sea ice edge, Seasonal Ice Zone Reconnaissance Surveys (SIZRS) aboard U.S. Coast Guard Arctic Domain Awareness flights were made monthly from June to October in 2012, 2013, and 2014. The seasonal ice zone (SIZ) is where sea ice melts and reforms annually and encompasses the nominally narrower marginal ice zone (MIZ) where a mix of open-ocean and ice pack processes prevail. Thus, SIZRS provides a regional context for the smaller-scale MIZ processes. Observations with aircraft expendable conductivity-temperature-depth probes reveal a salinity pattern associated with large-scale gyre circulation and the seasonal formation of a shallow (500 m) fresh layer moving with the ice edge position. Repeat occupations of the SIZRS lines from 728 to 768N on 1408 and 1508W allow a comparison of observed hydrography to atmospheric indices. Using this relationship, the basinwide salinity signals are separated from the fresh layer associated with the ice edge. While this layer extends northward under the ice edge as the melt season progresses, low salinities and warm temperatures appear south of the edge. Within this fresh layer, average salinity is correlated with distance from the ice edge. The salinity observations suggest that the upper-ocean freshening over the summer is dominated by local sea ice melt and vertical mixing. A Price-Weller-Pinkel model analysis reveals that observed changes in heat content and density structure are also consistent with a 1D mixing process.

1. Introduction

The Beaufort Sea seasonal ice zone (SIZ) is the area of the Canada Basin that lies between minimum and maximum annual sea ice extents. The SIZ encompasses the ice edge and the marginal ice zone (MIZ) as they move north and south each year in conditions ranging from full ice cover to open water. Based on this definition of the SIZ, its size is variable. In 2012, the September SIZ along 150°W reached northward of 80°N; in 2014, it extended merely to 75°N.

The variability of such an area and the fragility of the first-year ice it principally contains motivate the study of the underlying ocean, especially since the Beaufort Sea and Canada Basin account for the greatest recent loss in Arctic multiyear sea ice extent (Maslanik et al. 2011). This emerging influence of sea ice is due in part to the youth of the Beaufort Sea SIZ as we know it today; Comiso et al. (2008) note the marked retreat of the western Arctic ice edge relative to satellite-derived climatology, and Rabe et al. (2014) observe an increase of

freshwater storage contemporary with sea ice decline in many parts of the Arctic Ocean.

Seasonal Ice Zone Reconnaissance Surveys (SIZRS) is a program of repeated ocean, ice, and atmospheric measurements across the Beaufort Sea SIZ designed to track and understand the interannual variability of the SIZ. These measurements are taken aboard U.S. Coast Guard Arctic Domain Awareness (ADA) flights of opportunity using aircraft expendable atmosphere and ocean probes. They are designed to capture full air and water column properties in variable ice conditions spanning the SIZ. In addition to these sections, SIZRS buoy deployments provide continuous time series in several locations in the SIZ.

Hydrographic data gathered as part of SIZRS have shown that the summertime upper-ocean temperatures along the 1508W line above 50-m depth have increased up to 28C, and salinities (presented in this manuscript in psu) have decreased as much as 5 relative to summertime climatologies (Timokhov and Tanis 1997; Boyer et al. 2012; Johnson et al. 2012; Seidov et al. 2015). The SIZRS dataset enables us to quantitatively characterize this relationship through the Canada Basin and through the melt season.

As the SIZ distinguishes itself from long-term averages, a coherent pattern emerges in its behavior.

Corresponding author: Sarah Dewey, deweys@uw.edu

When the background gyre signal in salinity is removed, the salinity in the upper 20 m of the Beaufort Sea SIZ registers significantly with the ice edge, independent of year and latitude, and the seasonal appearance of an observed fresh layer relative to the edge is determined almost exclusively by the change in sea ice extent.

2. SIZRS observations

The SIZRS stations are typically at each degree of latitude at least from 72° to 76°N along the 1408 and 1508W lines of longitude in the Beaufort Sea. To capture the full extent of the SIZ, from open water to ice-covered areas, sampling in some years has extended farther north. The annual minimum ice edge in the western Arctic had already been retreating farther north (Drobot et al. 2008), but in September of 2012 ice extent was the lowest of the satellite record and SIZRS sampling extended to 808N, 1508W to reach sea ice.

SIZRS sampling times are designed to capture the full arc of the SIZ melt season, with repeat occupations of the survey lines each month. Sampling in 2012 began in May; in subsequent years sampling started in June to increase the likelihood of finding completely open leads free of new ice (more than minimal surface ice prevents the expendable probes from deploying properly). Sampling usually concludes in October, though the 2013 field season ended in August due to suspended federal government operations. Despite these gaps in temporal coverage, the SIZRS dataset offers unique in situ snapshots of the SIZ even during months of limited ship access. In this analysis we focus on the 1508W line because it has the most continuous record of observations and thus provides more information for analysis and modeling than the 1408W line, the occupation of which only began in 2013.

Instrumentation for the hydrographic portion of the SIZRS missions is a Tsurumi-Seiki (TSK) airborne expendable conductivity-temperature-depth (AXCTD) probe, first deployed in the Canada Basin as part of an International Polar Year hydrographic survey (McPhee et al. 2009) and similar to the Sippican instruments used in the Eurasian Basin by Childers and Brozena (2005). McPhee et al. (2009) compared AXCTD profiles to surface-deployed CTD profiles and found TSK AXCTDs salinities accurate to 0.02 and temperatures accurate to 0.028C. Probe depth is determined by fall-rate calculation and is accurate to 2% with a resolution of 0.11 m and a maximum depth of 1100 m; in the modeling portion of this present study, hydrographic data are smoothed to 1-m resolution to reduce instrument noise.

During the SIZRS ADA flights, the AXCTDs were dropped into open leads from C-130H Hercules aircraft flying at speeds of 60–70 m s²¹ and altitudes of 60–120 m.

Data were transmitted in real time to one of the aircraft's antennae as a 172-MHz FM radio signal, converted to engineering units by a TSK converter, and recorded on a laptop computer. The raw telemetered data stream is also archived on a solid-state sound recorder. Comparisons with ice-tethered profiler (ITP) data (http://whoi.edu/itp), UpTempO data (http://psc.apl.washington.edu/UpTempO/), and with ship cruise data (http://www.whoi.edu/website/beaufortgyre/data) indicate no significant differences between our full-depth profiles and those in similar Arctic ice conditions.

3. Observational analysis

The evolution of temperature and salinity along 1508W during 2014 was typical of SIZRS seasons. Figure 1b shows how the surface ocean warms in response to receding ice cover in August and September and how that heat may be trapped as a near-surface temperature maximum (NSTM) with the onset of freezing in October. The summer Pacific Water layer is visible at 50–70-m depth.

As in each previous year, 2014s SIZRS salinity sections reveal the formation of a near-surface, low-salinity layer south of the ice edge, extending farther north following the ice edge (Fig. 1c) and growing deeper as the season progresses (Fig. 1a). This observation can be explained as the freshening of the near-surface layer by melting ice. A sample calculation of the change in freshwater content (FWC) between June and September 2014 at 748N, 1508W illustrates this. Following Carmack et al. (2008), we consider the FWC (m) to be

FWC_{ocean}
$$5 \int_{2}^{\delta_{20}} \frac{34:8 \, 2 \, S(z)}{34:8} dz$$
,

where salinity data are smoothed to 0.5-m-depth resolution, and the top 2 m of data are excluded to eliminate the effects on salinity measurements of any AXCTD sensor start transients or local lead effects. This is reasonable because, owing to mixing, we expect the salinity in the top 2 m to be nearly the same as the salinity at 2-m depth. While in the summertime central Arctic Ocean, a freshened surface layer can develop in the leads between ice floes under quiet conditions (Hayes and Morison 2008), SIZRS has not generally sampled under such conditions. In the early part of the SIZRS season there has been limited melt, and later in the season the very near surface is reasonably well mixed as the ice concentration decreases and floes move in free drift. However, as a test of the sensitivity of the FWC calculations to this assumption, we assume an extreme case where the 2 m is 0.5 less than the ambient mixed layer salinity, and the effect would be a reduction in FWC of 0.1 m.

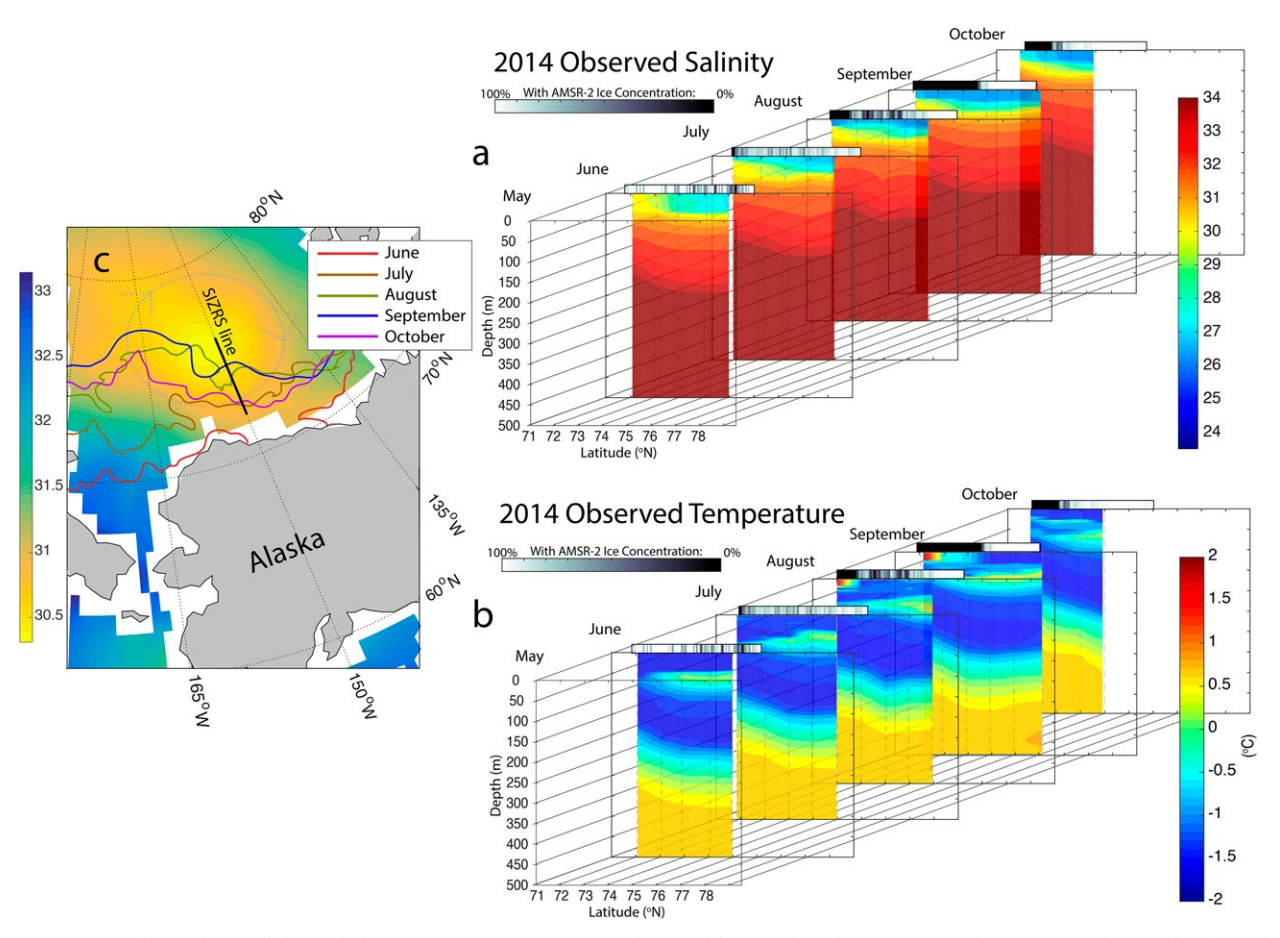


Fig. 1. Sections of (a) salinity and (b) temperature to 500 m are shown with overplotted AMSR-2 sea ice concentration on the date of deployment. (c) The SIZRS 1508W line is also shown in its regional context, against lines representing the 15% AMSR-2 ice edge average position for the week of each deployment in 2014, a dashed circle indicating the typical position and direction of the Beaufort Gyre, and summer climatological 30-m salinity from the PHC3.0 climatology (Steele et al. 2001) indicating the gathering of freshwater in the center of the gyre due to Ekman convergence.

The melt season change in FWC in the top 20 m of this station is taken as the difference between the September and June integrals. We assume a mean sea ice salinity of 10 and June and September ice thicknesses of 1.25 and 0.6 m, respectively, per Lindsay and Schweiger's (2015, see their Fig. 4) recent climatological study of sea ice thickness. Under this assumption, we calculate the FWC of the sea ice in equivalent meters of freshwater by multiplying sea ice thickness Hice by the local Advanced Microwave Scanning Radiometer 2 (AMSR-2) average sea ice concentration (SIC) for the week of each SIZRS measurement; this value is then scaled by the density ratio of sea ice to freshwater $(\mathbf{r}_{ice}/\mathbf{r}_{FW})$ and sea ice salinity Sice to estimate the amount of freshwater yielded by melt:

$$\mathrm{FWC}_{\mathrm{ice}} \; 5 \frac{r_{\mathrm{ice}}}{r_{\mathrm{nw}}} \; 3 \, \mathrm{H}_{\mathrm{ice}} \; 3 \frac{\mathrm{SIC(\%)}}{100} \; 3 \, (1 \; 2 \; \mathrm{S}_{\mathrm{ice}}) \, .$$

Thus, the FWC change (FWCC) of the ocean balances the loss of sea ice:

FWCC_{ocean} 5
$$\frac{\delta_{20}}{2} \frac{34:8 \ 2 \ S_{sept}(z)}{34:8} dz$$

2 $\frac{\delta_{20}}{2} \frac{34:8 \ 2 \ S_{June}(z)}{34:8} dz$ 5 1:04 m
FWCC_{ice} 5 $\frac{900 \ kg \ m^{23}}{1000 \ kg \ m^{23}}$ 3 0:6 m 3 0:049 12 $\frac{10}{1000}$
2 $\frac{900 \ kg \ m^{23}}{1000 \ kg \ m^{23}}$ 3 1:25 m 3 0:996 12 $\frac{10}{1000}$

Any difference between the FWC values of the melting ice and the upper ice-free ocean replacing it could be attributed to horizontal advection or uncertainty in the values of sea ice salinity, thickness, or concentration.

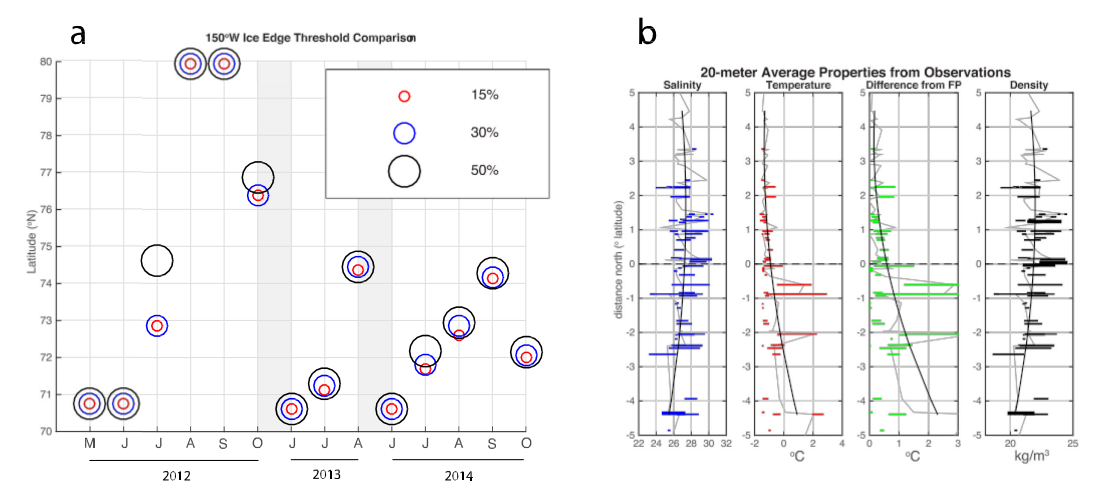


Fig. 2. (a) Comparison of sea ice edges from SSM/I (2012) and AMSR-2 (2013–14) passive microwave products. Concentric circles indicate agreement in ice edge position between concentration thresholds. The largest disparities in ice edge position occur at the beginning and end of the SIZRS season, during the onsets of melt and freeze-up. The resolution of the SSM/I data is 25 km, and the AMSR-2 is 3.125 km. (b) The 20-m averages (gray) of salinity, temperature, difference from calculated freezing point, and density from all deployments on 1508W relative to the 15% ice edge. Thick black lines show a quadratic fit to the data, and colored bars display the full range of values at each distance. Average salinity values decrease both to the north and south of the ice edge, while temperature increases above the freezing point south of the ice edge. Variance in temperature is substantially greater to the south of the ice edge, as insolation heats open water, whereas salinity variance remains relatively consistent throughout the section.

Assuming 610, 60.2 m, and 610% uncertainties, respectively, the FWCC can change by 60.24 m.

The comparison is crude, but the difference between the freshwater input by the melting ice and the change in observed ocean freshwater content does have a difference of 4 cm. This difference suggests that 4 cm worth of freshwater from ice melt did not remain where the ice melted but was advected away. These very rough, observationally based estimates indicate that 96% of the SIZ salinity change is due to vertical mixing and that 4% is associated with horizontal advection and other processes that remove freshwater. Accounting for uncertainty in sea ice FWC, we find that this salinity change ranges from 81% to 100%.

Because of the first-order role of ice melt and the apparent relationship of surface salinity to distance north or south of the ice edge, it is useful to view the SIZRS data in a reference frame relative to the ice edge rather than to station latitude. To accurately locate the ice edge in a MIZ characterized by highly variable ice concentrations, we use weekly mean sea ice concentration from the AMSR-2 (2013 and 2014; 3.125-km resolution) and SSM/I (2012; 25-km resolution) passive microwave satellite data. The southernmost incidence of a threshold concentration is considered the edge. For 15%, 30%, and 50% threshold concentrations, ice edges are nearly indistinguishable at the resolution of the satellite products except during the onsets of melt in

July and freeze-up in October (as signified by the decrease and increase in sea ice extent along the 1508W section; see Fig. 1c and Fig. 2a). Because these products have trouble distinguishing melt ponds from open water, and may therefore underestimate sea ice concentration (Rösel and Kaleschke 2012), overlap of the 15% and 50% edges increases our confidence in having located an edge. We therefore use 15% concentration as the definition of the ice edge, in keeping with the National Snow and Ice Data Center definition of sea ice extent.

In quantifying the relationship of the surface layer to the ice edge, we look at the upper 20 m of the water column. This depth lies above sources of stored heat like the near-surface temperature maximum (Jackson et al. 2010) and Pacific Summer Water (Steele et al. 2004) and within typical mixed layer depth ranges for the Beaufort Sea and Canada Basin (Toole et al. 2010; Peralta-Ferriz and Woodgate 2015). To avoid overlap with these features, we consider the average properties above them, that is, 20-m mean salinity and temperature.

The upper 20-m mean temperatures plotted versus ice edge position defined above (Fig. 2b) support the idea of similar salinity patterns moving with the ice edge. They become highly variable south of the ice edge and stay consistently within 0.58C of the freezing point under the ice. While some portion of this heat could be from

warming Pacific inflow through the Bering Strait (Shimada et al. 2006; Woodgate et al. 2006), Steele et al. (2010) find that 77%–83% of surface layer warming in the Pacific Arctic comes from local radiative heating, and the contribution of Bering Strait inflow is limited to the southern Beaufort Sea nearest to the Alaskan coast. While Steele et al. (2010) perform this calculation for the upper 60 m of the water column, we will show one-dimensional model analysis with SIZRS data (see section 4) also supports local, predominantly solar warming in the upper 20 m.

The 20-m mean salinities for each station registered relative to the ice edge position (Fig. 2b) also reveal a pattern on the scale of the SIZ. The water reaches peak salinity slightly north of the ice edge and freshens away from the edge to the north and south. The location of the peak salinity is pushed northward in the late summer to early autumn months (August through October) as water to the south freshens due to ice melt.

The freshening well to the north of the ice edge indicates that melt is not the only influence on this 20-m mean salinity. This northern upper-ocean freshening is a component of the anticyclonic Beaufort Gyre circulation (Proshutinsky et al. 2009). Figure 1c illustrates the location of the Beaufort Gyre with the Polar Science Center Hydrographic Climatology (PHC) 30-m salinity climatology for winter (Steele et al. 2001) when the anticyclonic circulation is typically strongest, and a sketched circle represents the circulation pattern. The SIZRS upper-ocean salinity along 1508W (Fig. 3a) shows a minimum in the northern third of the section at the middle of the Beaufort Gyre. Two features stand out when SIZRS measurements are compared to the National Ocean Data Center (NODC) salinity climatology (Seidov et al. 2015; Fig. 3b): basinwide, the upper ocean is fresher in SIZRS observations and that freshening is greatest in the middle of the gyre and just south of the ice edge (Fig. 3c). It seems clear that the spatial variation in observed upper-ocean salinities results from a mix of SIZ signals and larger-scale influences largely independent of ice edge position and associated with the Beaufort Gyre.

In the anticyclonic Beaufort Gyre system freshwater is gathered at the midbasin (e.g., Proshutinsky et al. 2009) by Ekman transport convergence of near-surface water by the anticyclonic winds of the Beaufort high. North of the ice edge, the meridional gradient in our observed 20-m average salinities is an expression of the upper-ocean freshening and surface doming of the Beaufort Gyre (Fig. 4b). The center of the gyre varies slightly with time but lies between 72.48 and 74.48N and 1398 and 1518W according to satellite-derived dynamic ocean topography (Morison et al. 2012; Giles et al. 2012) and

at 73.58N and 1438W from in situ observations (Proshutinsky et al. 2009). Dynamic height calculations to a reference depth of 500 m using the Monthly Isopycnal/Mixed-Layer Ocean Climatology (MIMOC) and NODC climatologies (Johnson et al. 2012; Seidov et al. 2015) show the center of the Beaufort Gyre dome on 1508W falls at 748–758N; this center latitude aligns with the location of the minimum, SIZRS-observed, 20-m salinity, which falls between 738 and 758N (Fig. 4b). An increasingly negative salinity gradient in this latitude range indicates an increase in Beaufort Gyre doming and intensity.

We thus find that the salinity pattern associated with the ice edge is superposed on the gyre-scale salinity patterns. To more clearly show the ice edge salinity pattern, we must identify and remove the time-varying gyre signal without eliminating the ice edge signal. To achieve this separation, we seek metrics of the strength of the Beaufort Gyre and the associated salinity gradients that are independent of the near-surface salinity data themselves. For this we consider three proxies for gyre strength: the monthly Arctic Oscillation (AO) index, the tilt of isopycnals in the halocline, and the ocean bottom pressure near the middle of the Beaufort Gyre.

The AO is the leading principal component of monthly mean sea level pressure anomalies in the Northern Hemisphere (Thompson and Wallace 1998) taken here from the National Weather Service's Climate Prediction Center (http://www.cpc.ncep.noaa.gov/).

A quadratic fit to the 20-m average salinities for each section is used to create an array of northward salinity gradients at each latitude for all months. (The mean R² value for all of these monthly fits is 0.82, and the median is 0.92.) These arrays correlate significantly (_ 95%) at a 2-month lag with the monthly AO index (Fig. 4a), indicating that large-scale atmospheric processes do in fact control the overall shape of salinity across the gyre but that the oceanic response to atmospheric forcing is delayed.

The sign of the correlation between the northward salinity gradient and AO is negative to the south and positive to the north, inflecting between 748 and 758N. This sign change reflects the behavior of the gyre dome along 1508W. The sea surface height tendency of the Beaufort dome is the opposite of the salinities because the fresher water lies in the middle of the gyre. The correlation pattern of Fig. 4a indicates that as the lagged AO increases, the dome steepens and the northward salinity gradient to the south of the gyre center becomes more negative. To the north, the gradient becomes more positive. The opposite is true as the AO shifts to its low regime, so that the lagged AO is always negatively

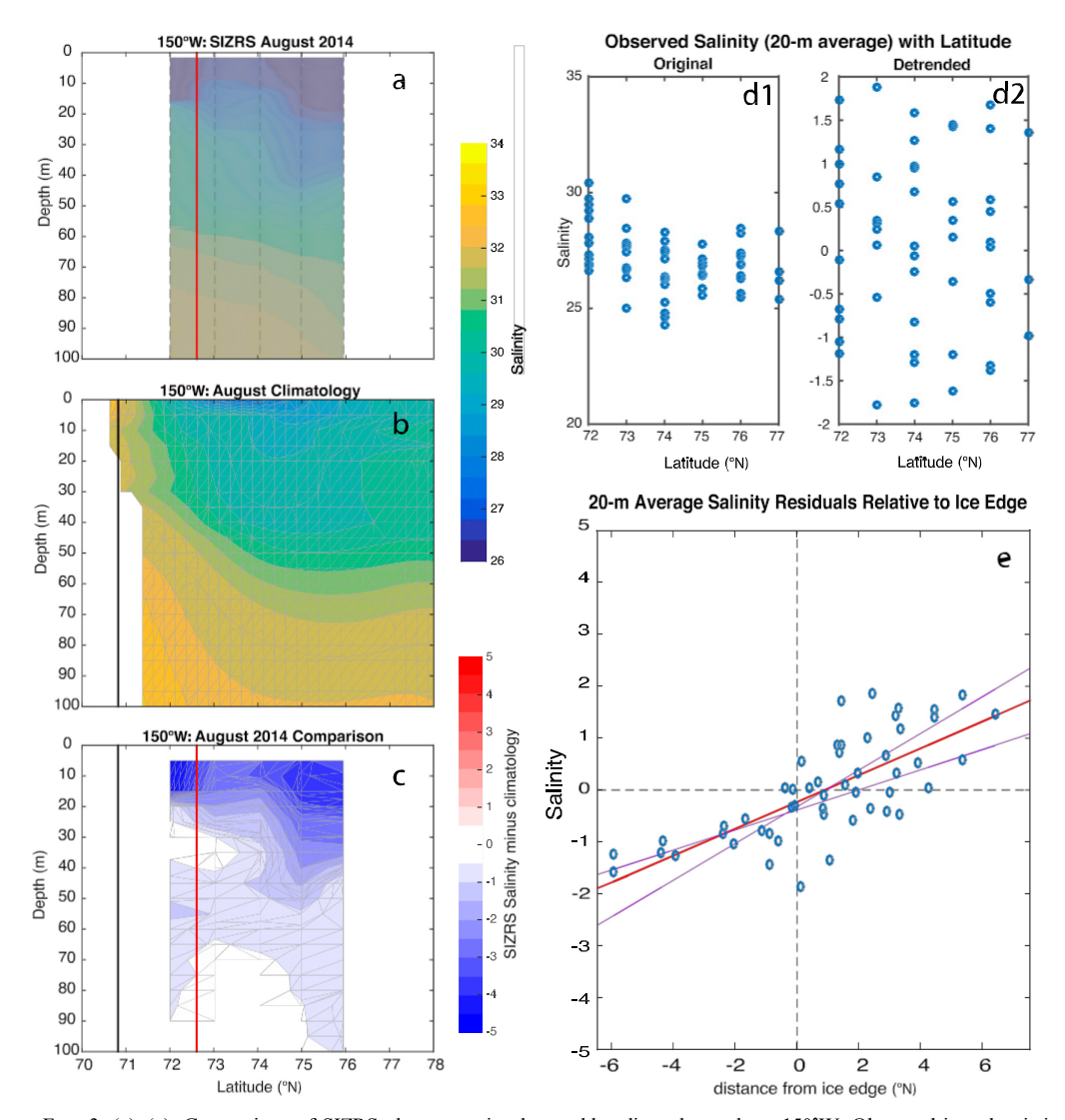


FIG. 3. (a)—(c) Comparison of SIZRS data to regional monthly climatology along 150%W. Observed ice edge is indicated in red; climatological ice edge is indicated in black. (Each employs a 15% concentration threshold, with the first using AMSR-2 passive microwave product and the second using NSIDC's monthly sea ice concentration climatology from passive microwave data; available online at http://nsidc.org/data/smmr_ssmi_ancillary/monthly_means.html.) SIZRS drop locations are shown with dashed gray lines in (a). The National Ocean Data Center climatology in (b) uses World Ocean Atlas data through the end of 2011. (c) The difference in salinity, when the climatology is subtracted from the SIZRS data. Areas of maximum freshening are found at the 2014 ice edge and at the center of the Beaufort Gyre (; 758N; see also Fig. 4). The 20-m average salinities from all months and all years vs latitude, (d1) before and (d2) after removing the gyre signal. (e) Salinity residuals after removal of the AO-correlated gradients are plotted vs ice edge distance. When the gyre signal is removed, residual values correlate significantly with distance from the ice edge. The blue circles show residuals from all SIZRS months in 2012–14; the red line is a linear fit to the data, and the purple lines are extrema for such a fit, generated in a 1000-iteration bootstrap simulation.

correlated with the salinity gradient south of 748–758N and positively correlated north of those latitudes. The correlation magnitude is significant everywhere except in the center of the gyre dome because the salinity gradient is always near zero at the center of the gyre (Fig. 4a).

The positive correlation between lagged AO and the strength of the Beaufort Gyre may seem counterintuitive, since high AO is generally associated with cyclonic circulation and the Beaufort Gyre is an anticyclonic feature. The reason for the positive correlation lies in the location of the center of action of the AO relative to

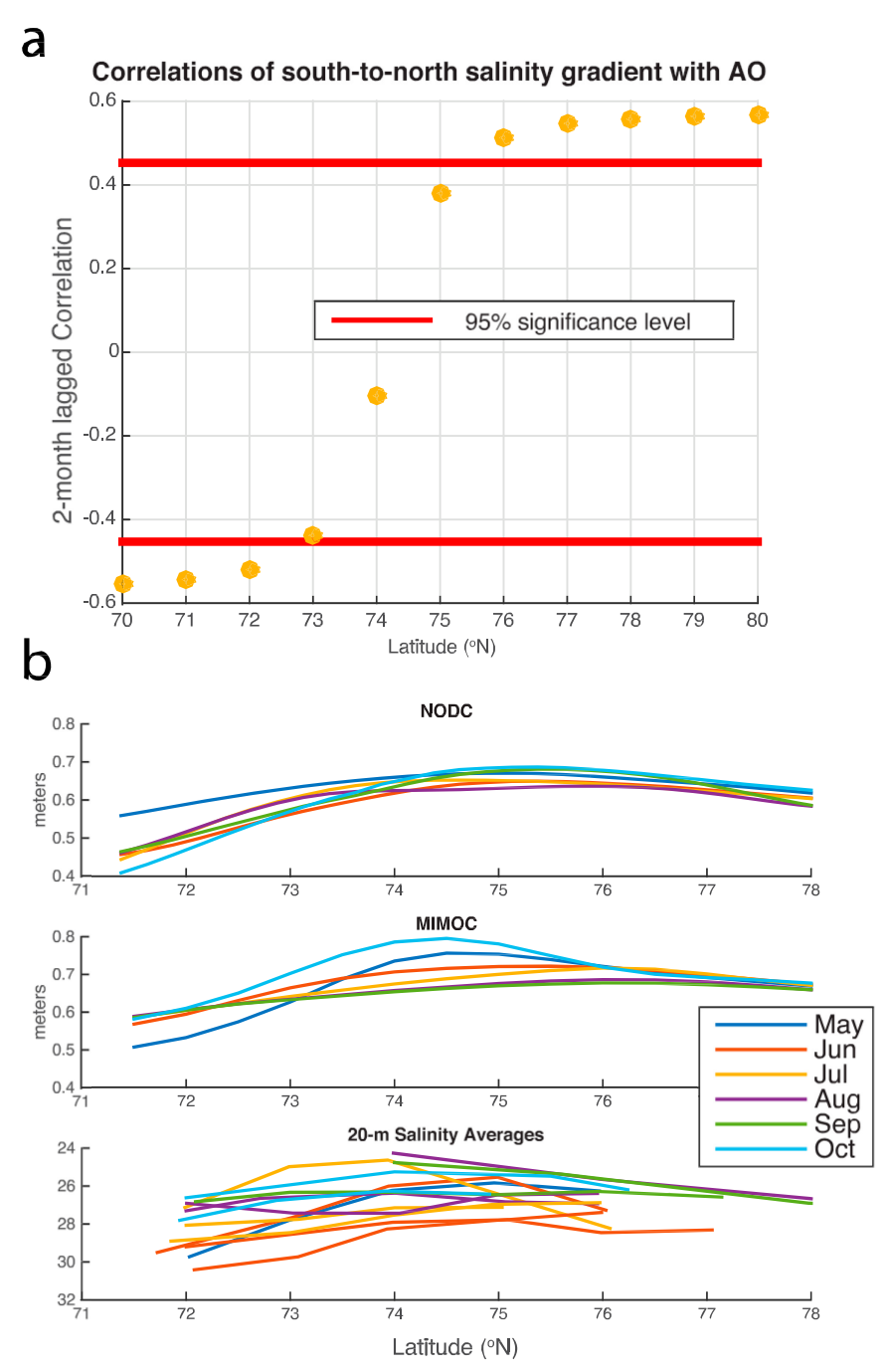


Fig. 4. (a) Correlations of a northward gradient in 20-m average salinities at each degree from 708 to 808N with the 2-month-lagged AO. (b) Comparison of dynamic heights calculated from NOAA and MIMOC monthly climatologies along 1508W. These heights indicate that the center of the Beaufort Gyre lies between 748 and 758N on 1508W. The 20-m mean salinities for every SIZRS monthly survey are shown in the bottom panel; the latitudes of peak salinity occur at or just south of the center of the gyre, as derived from calculated dynamic height relative to 500 m.

the Beaufort Gyre. Morison et al. (2012, their Fig. S1) extends to the northwest and includes the East Siberian have identified two expressions of the AO in the Arctic Sea; in a high-AO cyclonic regime, the Beaufort Gyre Ocean circulation. In an idealized low-AO anticyclonic is restricted to the central or eastern Canada Basin, regime, the anticyclonic flow of the Beaufort Gyre

and a cyclonic circulation dominates the Russian side of

TABLE 1. Correlation coefficients (r values) of salinity residuals with ice edge distance for each method. Bolded correlations have a p value less than 0.001. Here p value is the probability (0–1) that we would have collected the data we did had there been no relationship between salinity and distance from ice edge; the p value acts as a measure of significance for the correlation. The last two rows show the correlation of upper-ocean salinities to ice edge distance if a quadratic fit to the data is removed or if no fit is removed at all.

Gyre proxy	r				
	All data (May-October)	Autumn (August-October)	Spring (May–July)		
Lagged AO	0.73	0.77	0.67		
s _u 5 24 kg m ²³	0.58	0.64	0.31		
5 26 kg m ²³	0.57	0.62	0.25		
BGEP A (758N)	0.59	0.72	0.23		
BGEP B (788N)	0.59	0.72	0.23		
Quadratic south-north fit	0.13				
No signal removed	0.38				

the Arctic Ocean. This arrangement means that an increase in the AO results in strengthened northeastward wind stress on the northwest part of the Beaufort Sea and increased Ekman pumping of near-surface water toward the center of the Beaufort Gyre, and while the areal coverage of the Beaufort Gyre may decrease, its intensity increases (Morison et al. 2012). After a lag to allow the Ekman pumping to accumulate, this translates into increased freshwater content and doming of the gyre along 1508W.

The 2-month-lagged AO index may therefore be treated as a proxy for gyre strength and used to separate basin-scale salinity signals from the fresh wake of a retreating sea ice edge. A lagged regression of the standardized 20-m salinities onto monthly AO at each latitude through time gives the salinity value attributable to gyre effects. Subtracting this value from the measured salinities yields a set of salinity residuals that correlates significantly (Fig. 3e; Table 1) with distance from the ice edge. The ratio of the variance of these residuals to the variance of the 20-m average salinities is 0.6, so the residual salinity changes after removing the doming signal correlated with AO amount to $(0.6)^{1/2}$ or 77% of the total variability. This is slightly less than the 81%-100% variability we attribute to 1D processes based on earlier estimates but is reasonable considering that it represents an average including the northern part of the Beaufort Gyre not subject to the extreme surface fluxes of the SIZ.

Another proxy for gyre strength is the along-section slopes of two different isopycnals: s_u 5 24 and 26 kg m²³. These isopycnals fall between the depths of 10–60 and 90–140 m, respectively, during SIZRS sampling. Similar to the 20-m average salinities, the depths of the s_u 5 24 and 26 kg m²³ isopycnals follow a parabolic curve across the sampled latitudes. (For a quadratic fit, mean and median R² values for all monthly fits to the s_u 5 24 kg m²³ fit are 0.79 and 0.80, respectively; for s_u 5 26 kg m²³, they are 0.84 and 0.89.) We correlate

the slopes of these fits at each latitude with the meridional 0- to 20-m average salinity gradients. As in the AO correlation, these slopes correlate negatively with northward salinity gradients at lower latitudes and positively at higher latitudes, changing sign at 758N. We use a similar regression to that of the first (AO) case, replacing the monthly AO index with these isopycnal slopes and evaluating the correlation at zero lag. The residual salinity differences correlate significantly with distance from the ice edge (Table 1).

A third proxy for gyre strength is the Woods Hole Beaufort Gyre Exploration Project (BGEP) bottom pressure data (http://www.whoi.edu/beaufortgyre/data moorings.html) from moorings at 758 and 788N at 1508W. This ocean bottom pressure is related to gyre spinup at monthly time scales because circulation changes at these time scales include a strong barotropic component (Vinogradova et al. 2007). Raw ocean bottom pressure (OBP) data concurrent with SIZRS measurements are taken from the BGEP site (http://www.whoi.edu/ beaufortgyre/home) and detided using t tide (Pawlowicz et al. 2002). The time series are demeaned to account for mooring turnover in August of each year and correlated with monthly AO indices and with SIZRS 20-m average salinity gradients northward. The pressures correlate significantly with AO indices at a 2-month lag, though not significantly with the salinity gradients. When regressing these SIZRS northward salinity gradients at each latitude onto the pressure time series, the difference in pressures between the two pressure gauges is so slight (the meridional gradient is on the order of 0.01 millimeter per degree latitude) as to produce identical correlations between the residuals from this regression and the distance from the ice edge. OBP, like the other proxies, yields higher correlations in the fall than in the spring (Table 1), likely due to the enhanced role of early summer melt in changing surface layer salinity.

For each proxy, we can establish that the relationship of salinity residuals to edge distance is statistically sound by using the 1000-iteration bootstrap sampling of Efron (1979). A Monte Carlo test with replacement bootstrapping uses a probability distribution taken from the data rather than a normal distribution. The replacement of some values in the set with redundant values ensures that not all of the 1000 resamplings are identical and that the relationship to the ice edge holds when some data pairs are missing or duplicated. We run this bootstrap analysis on a linear fit to our plotted salinity residuals versus distance from the ice edge. This analysis generates upper and lower bounds for the linear fit (see purple lines on Fig. 3e for the AO proxy), showing that the relationship of salinity to edge distance is statistically robust and that the values of all salinity residuals from each proxy become more positive heading north. Standard errors in the slopes are minimal in the autumn case and at a maximum during spring runs, emphasizing again the role of melt in determining the presence of an ice edge-referenced fresh layer.

Using three different proxies for the strength of the background gyre, we have separated the signals of basin salinity and ice edge—influenced salinity. Having correlated monthly AO and bottom pressure to northward salinity gradients, we have shown that those parameters as well as isopycnal tilt may all be used to approximate gyre strength and yield the same general spatial pattern in salinity. Of the three proxies, the lagged AO delivers the strongest correlations (Table 1). This relationship only holds for salinity. The 20-m average temperatures do not correlate significantly with any of the gyre proxies used, a result that reinforces the role of local insolation in determining upper-ocean heat content.

4. Application of the PWP model to the SIZ

The relationship between salinity and distance to the ice edge and the correspondence of observed upperocean salinity change with observed ice melt suggest that ice melt and vertical mixing in the surface layer are the primary drivers of the evolution of SIZ salinity changes through the summer. This implies that horizontal advection is secondary; salinity changes are largely due to freshwater entering the ocean at the surface rather than being advected into the sites of the SIZRS stations from elsewhere. If this essentially 1D view of SIZ upper-ocean processes is true, it should also be reflected in the evolution of the thermal and density structure of the upper ocean, given reasonable estimates of surface thermal and stress forcing. Therefore, to test the hypothesis that 1D mixing processes are dominating the evolution of the SIZ upper-ocean structure, we develop and use a SIZ adaptation of the 1D mixing model of Price et al. (1986), hereinafter referred to as

the Price-Weller-Pinkel (PWP) model, to see if it can simultaneously account for the observed upper-ocean thermal, density, and salinity changes in the SIZ.

Our implementation of the PWP uses radiative, sensible, and latent heat fluxes; zonal and meridional surface stresses; and freshwater flux to make adjustments to the top cell of an ocean depth grid. Following the usual PWP formulation, at each time step, heat fluxes are first combined to calculate the thermal change to the top grid cell. Then freshwater fluxes are used to calculate a new salinity for the top grid cell. A density profile is computed and static instability is removed by mixing each cell with the one below it until the density profile is stable. After this stabilization, momentum from surface stress is added to the mixed layer cells at the top of the array (the mixed layer cells are those where the density difference between cells is less than 5 3 10²⁴ kg m²³). Velocities in the mixed layer are free to rotate at the inertial frequency. The array is then adjusted for stability at the base of the mixed layer by mixing the base cell and that just below it until they meet the threshold criteria for two different Richardson numbers. Mixed layer stability uses the bulk Richardson number, and shear flow instability uses the gradient Richardson number:

$$R_{\text{bulk}} \, 5 \frac{\text{gDrh}}{r_0 (\text{DV})^2}, \quad R_{\text{grad}} \, 5 \frac{\text{g>r/>z}}{r_0 (\text{>V/>z})^2},$$

where V is the horizontal velocity vector, h is the depth of the mixed layer, and deltas are taken to be the difference in values between the cell at the base of the mixed layer and the cell just below it. The adjusted arrays for temperature, salinity, and density are then saved and subject to the next time step's fluxes.

Sea ice presents a challenge in accurately estimating the surface fluxes that drive the PWP model simulations of polar oceans. Previous implementations of a high-latitude PWP (Hyatt 2006; Toole et al. 2010) have incorporated a flux law with summertime basal melting following Maykut and McPhee (1995) and a constant wintertime upward heat flux. We opt to use the output of a separate, three-dimensional ice-ocean model, the Marginal Ice Zone Modeling and Assimilation System (MIZMAS), to provide ocean surface fluxes. MIZMAS is a regional ice-ocean model derived from the Pan-Arctic Modeling and Assimilation System (PIOMAS; Zhang et al. 2008a,b).

We take the hybrid approach of using MIZMAS to drive the simpler 1D model for several reasons. While this approach cannot capture the ocean changes that stem from such things as the ice-ice and ice-ocean interaction and advective effects simulated by the much more complete and sophisticated MIZMAS model, it

serves to isolate the effect of 1D mixing. Because our explicit goal is to test the observation-based hypothesis that upper-ocean evolution during ice edge retreat is primarily a 1D mixing process, we do not want to cloud the conclusion with the possibility that more involved model physics are at play in the simulations. At the same time, even in this 1D view the surface forcing at one location varies with time according to the atmospheric forcing and the state and rate of change of the overlying ice cover. The surface stress, ice growth, and melt simulated by the more complete model drives our PWP runs without the requirement that we build a separate ice model or make many simplifying assumptions about ocean, momentum, heat, and salt fluxes.

In addition to limiting the physics to 1D mixing processes, the hybrid approach has the advantage that while MIZMAS provides the required forcing, PWP provides a more appropriate vertical resolution. MIZMAS has 40 ocean levels, and its resolution in the upper 77.5 m is 5 m, but we wish to resolve the mixed layer at a finer vertical resolution consistent with the 1-m vertical resolution of the observations obtained after smoothing 10-cm resolution raw data to reduce instrument noise. We are able to run the PWP at the same 1-m vertical resolution as our smoothed SIZRS observations.

MIZMAS' radiative fluxes and winds are forced by NCEP R-1, and the model assimilates sea ice concentration and drift to generate daily, grid cell-averaged fluxes as well as ocean profiles. For this investigation, daily fields for ocean surface heat fluxes and stress are interpolated to 3-hour increments. Since MIZMAS' curvilinear grid resolution is near 0.48 longitude and 0.048 latitude in the SIZRS region, the model grid cells closest to SIZRS AXCTD station coordinates are used for model forcing; forcing coordinates are chosen to fall at no farther than 0.258 from the station sites. While the spatial and temporal resolutions of MIZMAS are not optimal for running our 3-h model at one location, they represent the best available option for the continuous coverage and assimilated forcing needed to drive the PWP.

Initial temperature and salinity profiles are selected from SIZRS observations at our most often sampled latitudes at 1508W: 728, 748, and 768N. PWP runs are initialized with profiles that have no evidence of eddy activity and which have similarly clean profiles at the same station the following month. We define eddies as spikes in smoothed upper-ocean temperature or salinity at depths not associated with typical heat extrema (i.e., NSTM or Summer Pacific Water). These selection criteria allow for 19 separate 1-month model runs starting at different months spanning the duration of the SIZRS program. These 19 runs allow coverage of 1 month over

multiple latitudes as well as the same month in multiple years. For example, there are model runs starting in June in all 3 years as well as at multiple latitudes in each of those years (Fig. 5a). The model is run at 3-h time steps and 1-m depth resolution over the top 100 m of the water column. Background diffusivity is set at 10^{26} m² s²¹ per Guthrie et al. (2013) and in agreement with SIZRS-deployed airborne expendable current profilers (J. D. Guthrie 2016, personal communication), and optical attenuation coefficients are set to Jerlov oceanic type II (Jerlov 1976).

a. Taking surface fluxes from MIZMAS

While we use MIZMAS output to eliminate the need for an ice model on top of our PWP ocean, we adjust MIZMAS fluxes before feeding them into the PWP. These adjustments are motivated by comparison of MIZMAS and initial PWP simulation results with SIZRS observations, but we have tried to limit them to accounting for possible biases in underlying reanalysis products and the inherent differences between the MIZMAS and PWP model paradigms.

The accuracy of MIZMAS temperature, salinity, and other metrics are investigated in the model—observation synthesis portion of Zhang et al. (2016), which uses multiple observational datasets to evaluate MIZMAS in the Beaufort Sea region. To focus here on the SIZ surface layer properties, comparisons of MIZMAS simulated to SIZRS-observed month-to-month changes in upper-ocean temperature and salinity are illustrated in Fig. 5b for the periods shown in Fig. 5a. The average of the differences between MIZMAS and observed profiles over the 19 1-month periods are plotted with plus or minus one standard deviation.

Pertinent to the heat flux for PWP in the SIZRS periods, comparisons with SIZRS-observed month-tomonth temperatures (Fig. 5b) indicate that MIZMAS predicts temperatures approximately 0.58C cooler than observed at the surface. However, MIZMAS temperatures are 0.58C warmer than observed at the bottom of the summer mixed layer around 20-m depth in the NSTM, whose formation is a primarily 1D phenomenon (Steele et al. 2011) driven by radiative heating. With respect to salt flux, MIZMAS salinities are frequently over 1 higher than observations in the mixed layer in the months considered (Fig. 5b), comparable to the mean salinity 0.65 bias in the upper 100 m found in the two profiles considered in Zhang et al. (2016, see their Fig. 4).

b. Heat flux

We seek refinements to MIZMAS-derived flux inputs to PWP that are based on known biases in the reanalysis

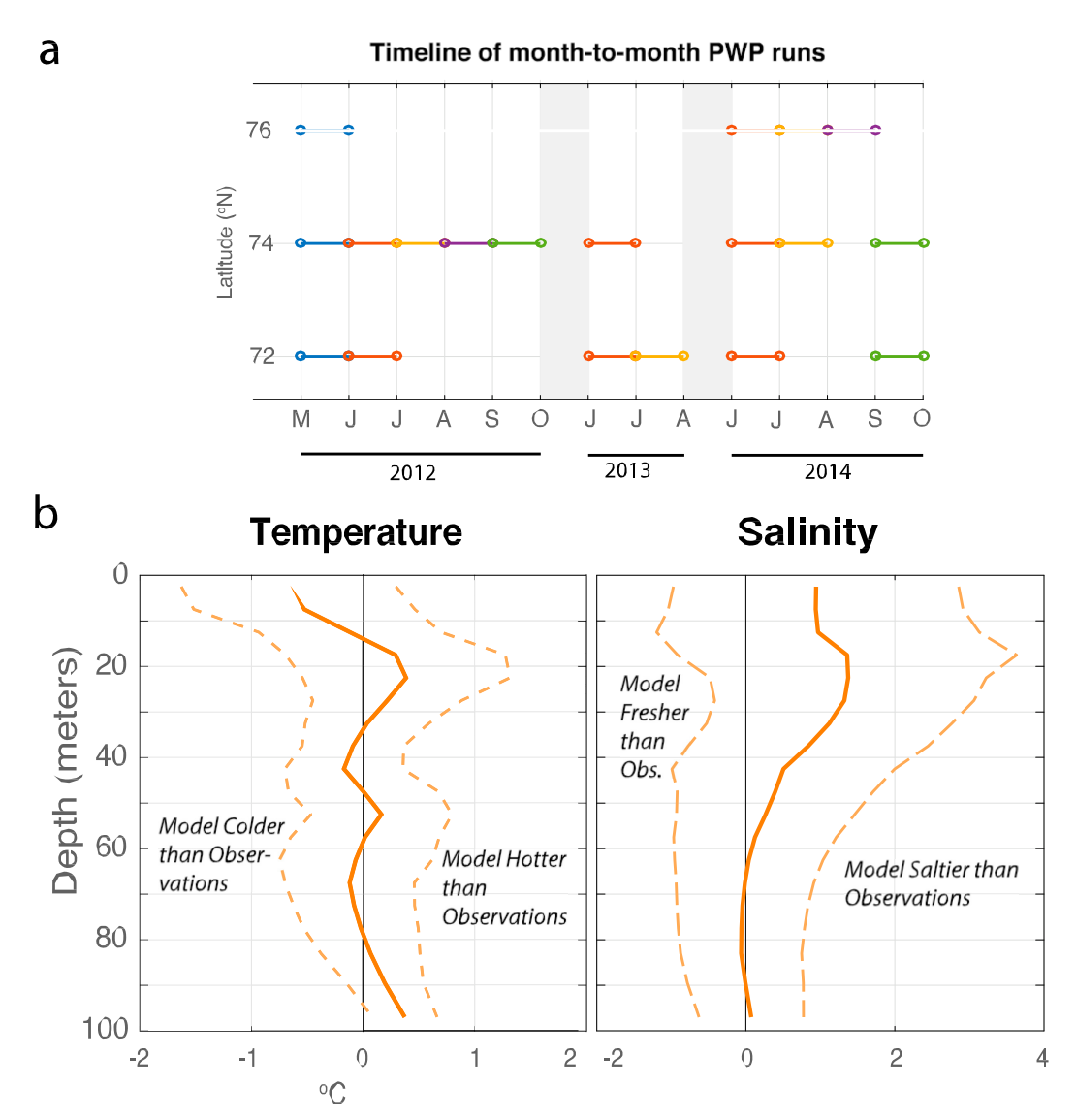


Fig. 5. (a) Months, years, and latitudes for each of the 19 PWP runs on 1508W, color-coded to correspond with the months shown in Fig. 4b. (b) Mean temperature and salinity differences between MIZMAS and observations over all depths and all months, plotted with plus or minus one standard deviation (dashed lines).

products that drive MIZMAS or clear requirements imposed by the inherent differences between PWP and MIZMAS. In the case of heat flux, we think the excess heat deep in the mixed layer and deficiency of temperature near the surface shown by MIZMAS (Fig. 5b) are due to the combination of too much overall solar heating of the mixed layer and relaxation to a 21.88C fixed freezing point temperature at the ocean's surface in the presence of ice (Zhang et al. 2016). The former factor suggests adjustments to MIZMAS forcing that affect surface heating are necessary to the implementation of the 1D PWP model.

The first adjustment is to remove an apparent bias due to the reanalysis input to MIZMAS, and then we subtract any ocean surface heating that goes directly to basal ice melt. The SIZRS timeline primarily covers the sea ice melt season, during which solar shortwave radiation exercises the principal control on bottom melting in areas of reduced ice coverage, and the role of longwave radiation is diminished (Perovich et al. 2011). Sensible and latent heat fluxes are much smaller than these radiative fluxes, and so we treat them as low-order contributions and do not adjust those inputs to PWP. However, Lindsay et al. (2014) have shown that NCEP R-1 shortwave radiation is biased as much as $100 \, \mathrm{W \, m^{22}}$ above observed values during the SIZRS sampling season. Using the average bias for the starting month of each PWP run from Lindsay et al. (2014, see

their Fig. 2), we subtract these values from our short-wave time series.

In addition to removing bias, we must account for the partition of ocean surface heat flux between basal ice melt and ocean heating. Sensitivity analyses of the PWP model in ice-covered conditions without this accounting produce surface warming up to 68C above observations. Perovich et al. (2011) show that across different ice concentrations and locations, 89% of shortwave radiation in the surface ocean typically goes to bottom melt of the overlying sea ice. MIZMAS, with its ice layer, accounts for this partition, but our ocean-only PWP cannot. Using the SIC from MIZMAS, we can account both for the ice melt and for the shortwave bias in one equation:

This scaling results in a total reduction of shortwave input to the PWP ocean surface heating of 50%–80%, consistent with the range of reduction Perovich et al. (2011) observed in their analysis of a Beaufort Sea ice mass balance buoy. While this range is large and susceptible to error, it represents a best estimate of what a realistic shortwave input may be.

c. Momentum flux

In our approach to momentum flux forcing for the PWP model, we do not have to modify MIZMAS surface stress for ice concentration, but similar to heat flux, we do scale surface stress inputs to account for reanalysis bias. During the SIZRS season floes move in near free drift, a condition in which internal ice stresses are negligible, so this ice regime has the potential to transfer most of the wind stress into the surface of the liquid ocean, without substantial change in magnitude (Martin et al. 2014). That is, if we consider the MIZMAS stress balance to be t_{ocean} 5 t_{air} 1 F_i as stated in Martin et al. (2014), where the Coriolis contribution to this force balance is ignored, and we consider the ice interaction force F_i as negligible in the MIZ per Hibler (1979), virtually all the momentum imparted by the wind to the ice or open-ocean surface is ultimately transferred into the upper ocean. MIZMAS surface ocean stress includes stress from open-water as well as ice-covered regions, and it accounts for the difference in momentum transfer over the two types of surfaces. For these reasons, we do not make stress adjustments based on ice concentration.

We do, however, scale the magnitude of the spatialaverage surface stress. Initial sensitivity analyses of PWP suggested that the MIZMAS-derived surface stress was insufficient for PWP to replicate observed mixed layer deepening. One reason for this is an underlying bias in wind speed used to drive MIZMAS. MIZMAS wind forcing is derived from NCEP R-1 (Kalnay et al. 1996), which can underestimate observed mean wind speeds by 25% (Lindsay et al. 2014). The PIOMAS and MIZMAS air-ice drag law is adjusted slightly to best match modeled ice velocity to drifting buoy ice velocities over the whole Arctic Ocean. This would account for bias in the reanalysis winds except in the SIZ where ice concentration can be low and the wind stress on open water accounts for a greater percentage of the aggregate momentum transfer. We assume that the mechanical forcing over the SIZ mix of open water and sea ice should scale with the square of wind speed. We therefore increase PWP surface stress forcing by scaling up MIZMAS aggregate ocean surface stresses by multiplying by 2.29 5 1/(1 2 0.25)² to account for this wind speed bias. This adjustment increases PWP surface layer mixing and results in a mixed layer evolution that better agrees with observations.

d. Salt flux

We derive the surface buoyancy, proportional to salt flux, for PWP from MIZMAS ice melt. Because sea ice is fresher than seawater (; 10 bulk salinity for sea ice vs 30 for seawater) sea ice melt produces negative salt flux and positive buoyancy flux downward. Conversely, sea ice formation produces salt and negative buoyancy flux downward. MIZMAS produces ice thickness estimates that agree with observations (Lindsay Schweiger 2015) and are consistent with sea ice changes over the summer in the Beaufort Sea. Therefore, to assess the month-to-month contributions of ice melt and formation to upper-ocean salinity, we calculate the freshwater flux as FWC change, in meters per second, due to area-averaged MIZMAS ice volume melt over each station's latitude. This calculation uses the satellite remote sensing-derived sea ice concentration (see SIZRS observations) times the change in MIZMAS ice thickness, with an assumed sea ice salinity of 10 consistent with first-year ice. This method allows us to calculate total freshwater drainage from the sea ice without having to parse the contributions of top and bottom ice melt. The method provides a higher spatial resolution estimate of sea ice concentration than the MIZMAS cell-averaged value. This increased resolution is useful close to the ice edge. The change in ice cover from 1 month to the next is divided evenly over time steps in the PWP run, resulting in a salt/freshwater flux that is constant over a month. While this smoothing does not capture the typically spatially varying nature of brine release from ice growth in leads (Nguyen et al. 2009), it

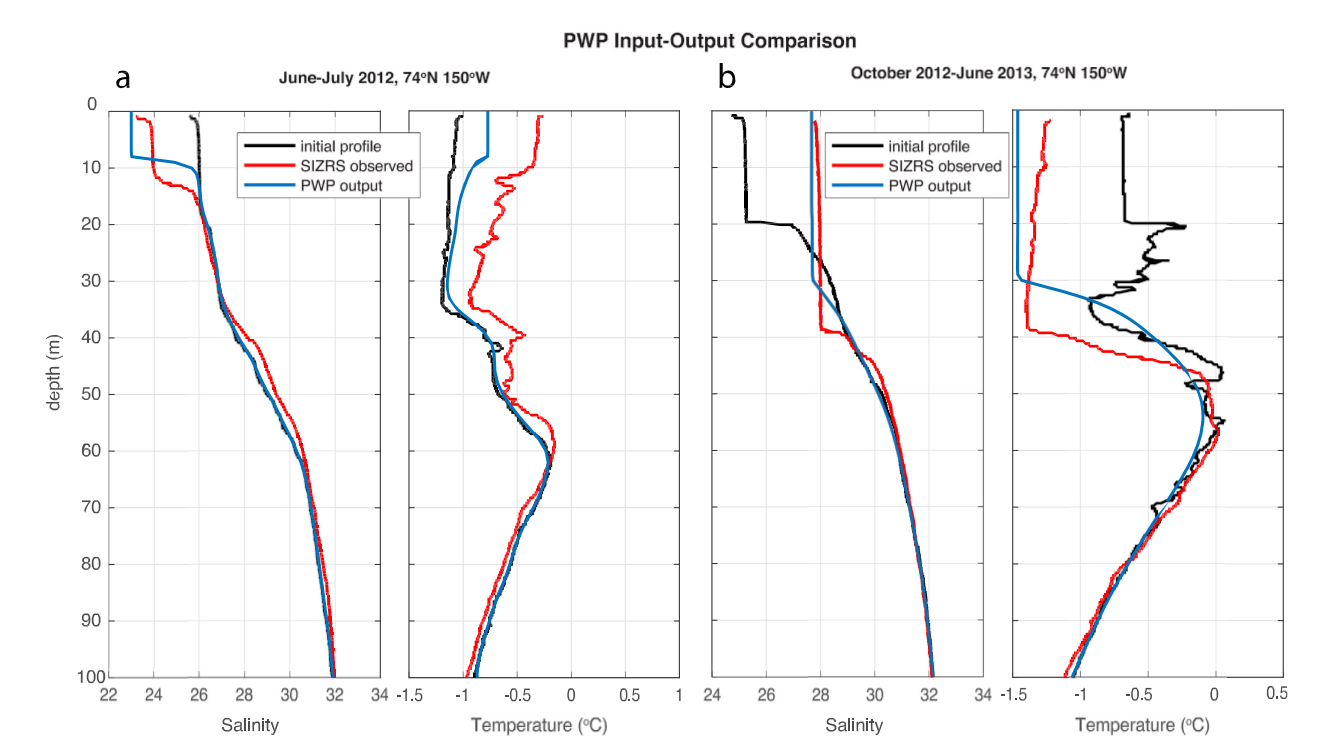


FIG. 6. Examples of the (a) early summer shoaling and (b) overwinter deepening of the mixed layer in month-to-month PWP runs from June–July 2012 and October 2012–June 2013 at 748N, 1508W. Black lines indicate the observed profiles used to initialize the PWP, and blue lines indicate the PWP output. Red lines are the observed profiles contemporaneous to the blue lines.

can adequately describe the more spatially uniform release of freshwater due to seasonal melt.

5. Results from observations and the PWP model of the SIZ

Examples of month-to-month transitions in upperocean observed and simulated changes (Fig. 6) indicate that the PWP model and observations behave qualitatively as we expect during summer and winter periods of ice melt and formation. After 1 month of observation is used to initialize the PWP, the model's output can be easily compared to observations from the following month in the same location. Example month-to-month PWP simulation results for early summer melt (Fig. 6a) and late summer/overwinter freeze-up (Fig. 6b) illustrate that the model can at least qualitatively capture the range of mixed layer behaviors we expect to see over the SIZRS season. In early summer, for example, June to July 2012 (Fig. 6a), the surface meltwater flux downward increases stratification that limits deep turbulent motransfer and results in development of a freshened shallow mixed layer, 12 m deep in the observations and 8 m deep in the PWP simulation. This mixed layer salinity freshens by about 2 in both observations and PWP simulations. Solar heating warms

the shallow mixed layer by an observed 0.758C. The modeled upper ocean warms in the new mixed layer, although less than observed, but as in the observations, the modeled warming extends down to 25 m, suggesting some radiant energy penetrates deeper than mechanical mixing.

The opposite is true of an overwinter run from October 2012–June 2013: downward freshwater (buoyancy) flux transitions from positive to negative resulting in near neutral to unstable stratification for which surface stress causes deepening of the mixed layer to 38 m (observed) and 30 m (PWP) from its shallow, 20-m, late summer state (Fig. 6b). The mixed layer also becomes almost 3 saltier in both the observations and PWP simulation as sea ice forms. Driven by wintertime cooling of the surface ocean, the observed and modeled mixed layer temperatures decrease by about 0.758C to near the salinity-determined freezing point.

Considering all 19 month-to-month PWP simulations, the agreement with observations varies, but as indicated by the ensemble averages of the differences between PWP and observations, average agreement is reasonably good (Fig. 7). Over the upper 100 m of the water column, the ensemble average bias of the PWP temperature changes relative to the observed temperature changes is 20.058C, and the standard deviation, averaged over 100-m depth, of

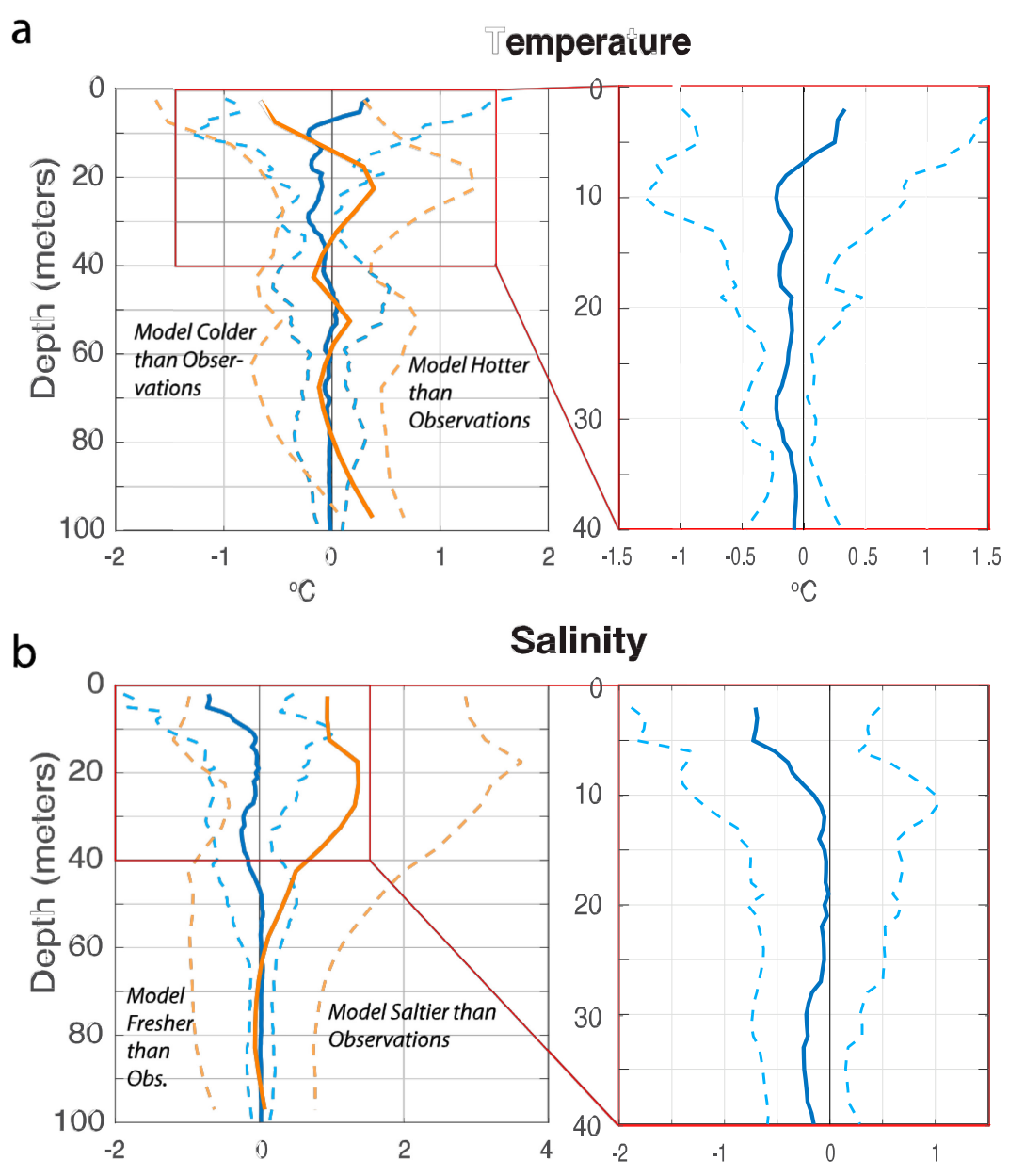


Fig. 7. Mean (a) temperature and (b) salinity differences between PWP and observations (blue) and MIZMAS and observations (orange) over all depths and all months, plotted with plus or minus one standard deviation (dashed lines). The top 40 m of the PWP differences are shown in the red boxes.

model biases relative to observations is 0.388C (Fig. 7a). The magnitude of this standard deviation in the upper 20 m is comparable in magnitude to the temperature variability observed south of the ice edge (Fig. 2b). The maximum ensemble average bias is 0.348C in the upper 5 m. Similarly, over the upper 100 m, the ensemble average bias of the PWP month-to-month salinity changes relative to the observed (Fig. 7b) is 20.08, and the standard deviation averaged over depth is 0.43. The maximum ensemble average bias is 20.73 in the upper 5 m.

These PWP-simulated biases relative to observed month-to-month changes are smaller than the departures of the MIZMAS temperature and salinity changes from the observed month-to-month changes. In the sense that MIZMAS is a simulation over a longer period of time than the month-to-month PWP simulations, this comparison is a little unfair. However, as discussed above, the MIZMAS temperature and salinity biases are likely partly due to biases in the NCEP reanalyses used to drive MIZMAS. Indeed, if we drive PWP with MIZMAS

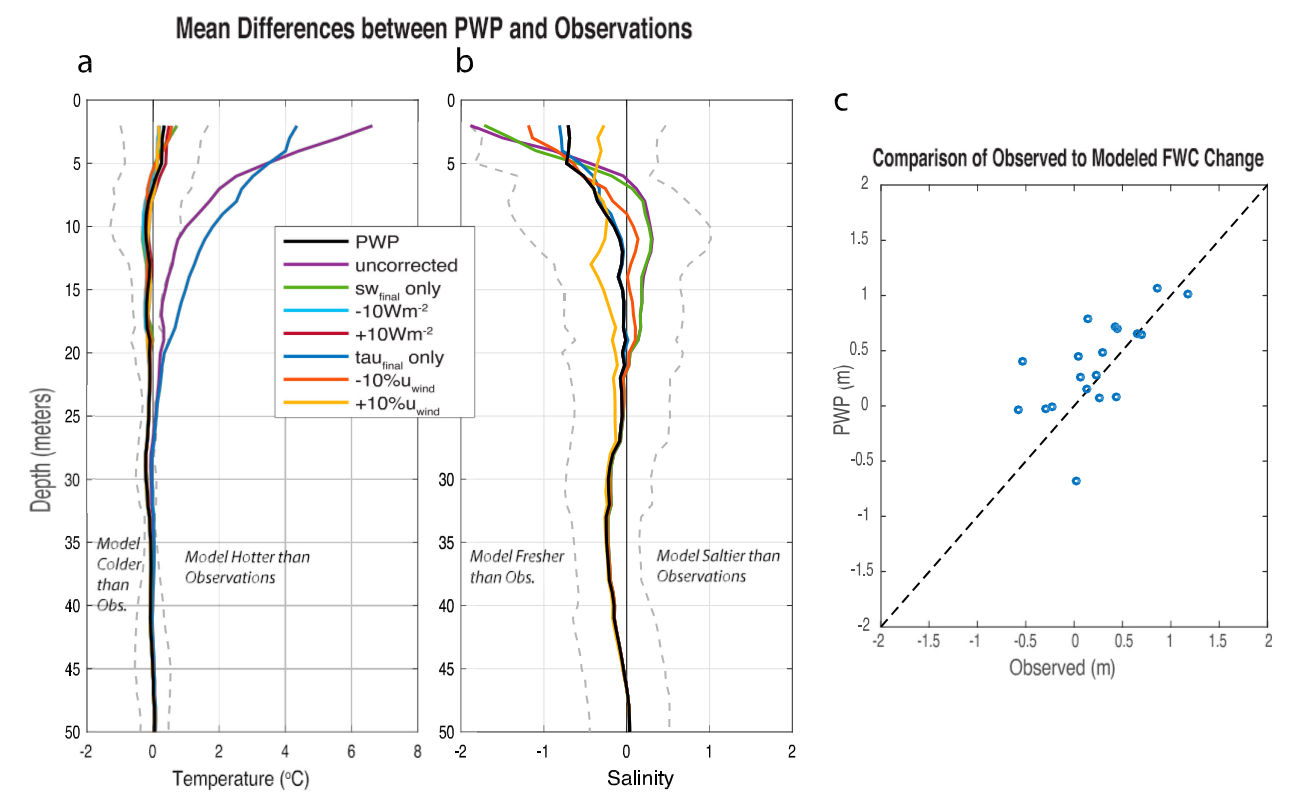


FIG. 8. Mean (a) temperature and (b) salinity differences between PWP and observations over all depths and all runs with adjustment of shortwave and surface stress forcing. Eight different scenarios are considered: one in which no changes to forcing are made, one in which only the shortwave input is changed, one in which only the surface stress is changed, and two each where the bias adjustments based on Lindsay et al. (2014) are increased or decreased about the final value for one forcing while the other is held constant at its final value. The eighth scenario is the final PWP output, flanked by one standard deviation (dashed lines). (c) Comparison of freshwater content change relative to 34.8 in PWP simulations and SIZRS observations. Change in meters is shown against a 1:1 line, with the majority of the PWP FWC change slightly in excess of that found in observations. These changes are consistent with earlier estimates of the FWC of sea ice and the underlying oceanic change. Because the ratio of its mean FWC magnitude to that of observations is approximately 1.13, the excess freshwater from the PWP is likely advected away.

forcing but no correction for NCEP biases (Fig. 8a), PWP, like MIZMAS, ends up with too much heat (28–68C) in the upper ocean (in MIZMAS this effect is reduced by fixing the temperature to 21.88C at the surface). Similarly, without correcting upward the input forcing of stress, the PWP near-surface stratification is higher than observed; salinities are too low near the surface and too high deeper in the mixed layer (Fig. 8b).

In addition to the PWP runs with the corrected MIZMAS shortwave heating, stress, and freshwater flux, we have run several sensitivity studies to demonstrate the relative importance of shortwave heating and surface stress in the PWP implementation (Figs. 8a,b). Eight different ensembles of 19 runs each are conducted in addition to the primary PWP ensemble with corrected MIZMAS-based forcing. The first run makes no corrections to MIZMAS shortwave or stress inputs. As discussed above, this arguably yields results most comparable to MIZMAS because the fluxes are not

adjusted for reanalysis biases. In the second example only the shortwave input is corrected, and in the third only the surface stress is corrected. Without any corrections to forcing (including both the scaling of shortwave heat and the removal of bias), PWP yields a surface temperature bias of 168C (Fig. 8a) and a salinity bias of 21.7 (Fig. 8b). Changing only the shortwave input makes the PWP temperature profiles more closely match SIZRS observations, but it results in an average salinity bias of 21.5 at the surface (Fig. 8b). Likewise, changing only surface stress yields a salinity profile close to observations but a temperature bias of 148C (Fig. 8a).

To understand the interplay between the two primary forcing adjustments, we include two runs in which the shortwave forcing has been varied while the surface stress input to PWP is consistent with the primary PWP ensemble and two runs in which the surface stress has been changed while the shortwave forcing correction remains

the same. Adjustments of shortwave bias by 10 W m²² about the corrected value result in little change from the primary result, whereas adjustments of surface stress by 10% result in changes in near-surface stratification (Figs. 8a,b). In each case, these changes are small relative to the primary corrections, reinforcing the physical assumptions that led to those corrections.

6. Vertical mixing versus advection in the SIZ

With respect to the question of the relative roles of vertical mixing versus advection, perhaps the most telling result of these analyses is the slight negative bias in average PWP salinity month-to-month change (Fig. 7b) and associated total FWC changes relative to observed changes. Arguably the negative bias in observed salinity change is at least partly due to advection not represented in the model, and the ratio of FWC bias to total FWC change is a potential measure of advection as a fraction of the total change attributable to mixing.

As shown in Fig. 8c, the PWP model is able to reproduce the freshwater content change integrated between 2- and 20-m depth. The 2-m upper limit eliminates the effects on salinity measurements of any AXCTD sensor start transients. As in our sample calculation at the beginning of this manuscript, a reference salinity of 34.8 is used for freshwater content calculations, following Carmack et al. (2008) and Aagaard and Carmack (1989). Estimated errors from this FWC calculation are on the order of 10²⁴ m.

The ratio of the mean magnitudes of FWC change in the PWP simulations to FWC changes in the observations is approximately 1.13, with a standard deviation in each of 0.3 m, suggesting 1D vertical mixing of sea ice melt can account for about 87% of upper-ocean freshening in the SIZ with on the order of 10% of freshwater being advected away. This result is similar to the back of the envelope calculation based on observations alone, 81%–100%, and the portion of salinity variability across the Beaufort Gyre not associated with variations in gyre circulation, 77% (e.g., correlated with the AO).

7. Interseasonal robustness of the PWP and the wintertime role of horizontal advection

Although it is not the focus of this work, an important question is the role of 1D mixing to wintertime evolution of the Beaufort Sea SIZ region. Does the formation of seasonal ice cover and the associated negative freshwater flux drive wintertime upper ocean changes through vertical mixing to the same degree that melting and positive freshwater flux does in the summer? We explore this question by simulating the transition from fall to late spring using our PWP-driven model by growth of the ice cover.

We have conducted runs of the PWP from October 2012 to June 2013 and August 2013 to June 2014 at 728, 748, and 768N at 1508W (Fig. 9). Generally, model-simulated mixed layer temperatures are within 0.258C of observations, and model-simulated salinities are within less than 1 (Fig. 9). However, in the case of the 2013–14 run, the PWP predicts a mixed layer fresher than observations by 2 at 768N.

Considering the variances of the difference between simulated and observed overwinter salinity changes, we find that the change in salinity shown by the model accounts for _95% of the variance in the observed overwinter salinity changes (Table 2). While the model does closely approximate mixed layer depths in the majority of runs, in others it can underestimate the depth by up to 15 m. This difference may be due to the temporal resolution of the PWP surface stress forcing. The depth of wintertime mixing tends to scale with u*/f, where u* is the friction velocity, and f is the Coriolis parameter (e.g., McPhee 2008). The surface stress forcing interpolated from daily MIZMAS surface fluxes likely does not capture the peak stresses and maximum mixed layer deepening associated with winter high-wind events. Indeed, the SIZRS scenario differs from that described by Fer et al. (2017) in their 1D analysis of wintertime change in the Nansen Basin. They find that entrainment from below the mixed layer, rather than brine rejection, dominates the salinity changes therein. This contrast likely reflects the difference between the Eurasian Basin SIZ, characterized by outflowing ice underlain by inflowing warm, salty Atlantic Water (e.g., Untersteiner 1988), versus the Beaufort Sea SIZ, characterized by ice and a relatively stable surface layer trapped in an anticyclonic gyre circulation and isolated by a cold halocline from Atlantic Water heat below.

Our salinity results indicate that the majority of freshwater content change in the upper ocean in the Beaufort Sea comes from vertical fluxes that originate with local sea ice melting and formation, suggesting that the contributions of freshwater surface horizontal advection are small relative to vertical 1D processes. To independently estimate the contributions of horizontal advection to surface freshwater distribution, we have calculated advection in MIZMAS using the dot product of velocities and smoothed salinity gradients gridded onto a rectangular 0.28 longitude by 0.18 latitude matrix, bounded by 1558W, 1358W, 808N, and 708N. We use this advective salt flux (kg m²³ s²¹) to calculate convergence at each grid point in order to estimate a cumulative salinity change over each SIZRS season.

We find the MIZMAS-derived horizontal salt flux convergence to be $O(10^{28})$ to $O(10^{29})$ kg m²³ s²¹ averaged on 1508W between 728 and 768N. When we compare

PWP output comparisons with observations

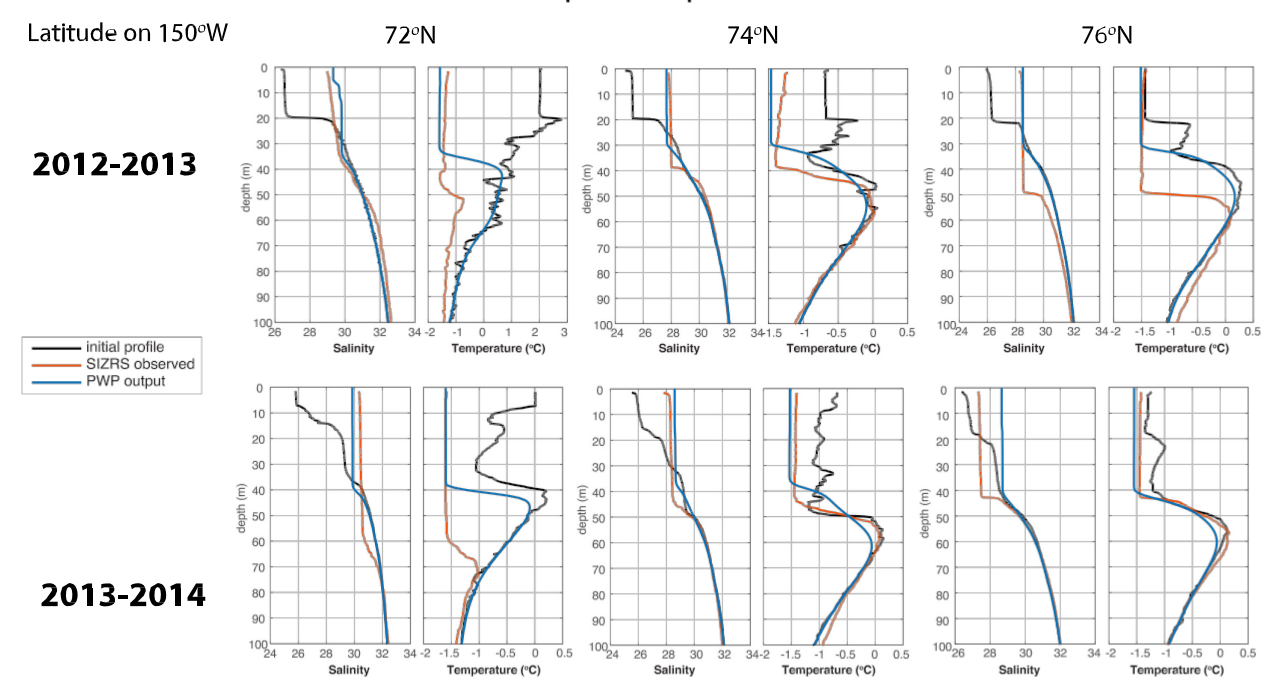


Fig. 9. PWP runs on three latitudes from October 2012–June 2013 and August 2013–June 2014. Black lines are the profiles of temperature and salinity used to initialize the PWP run, and blue lines are the PWP output. Red lines are the observations contemporaneous with the end of the PWP run; the success of the PWP is determined by the resemblance of the blue lines to the red.

the advective change to that from vertical freshwater fluxes, the expected change in salt content per cubic meter, O(10²¹) kg, is approximately one order of magnitude smaller than that expected from melting 1 m³ of ice, O(10) kg, over 6 months. For example, advection of 2 3 10²⁹ kg m²³ s²¹ yields 0.31 kg of salt per cubic meter in 6 months. This translates roughly to a salinity change of 0.3, 20% of the surface salinity change from June to September 2014 at 748N, 1508W of approximately 1.5. These results are consistent with the 10%–20% residual role for advection estimated from observations and comparisons of PWP results with observations.

8. Discussion

Observations in the Beaufort Sea SIZ indicate a characteristic pattern of upper-ocean freshening aligned with the retreating ice edge position. This behavior can be seen in the SIZRS data at a basin scale—melt occurs everywhere—and the resulting freshening is apparent throughout the gyre but most prominently south of the ice edge where ice has completely disappeared (Fig. 1) and associated cumulative surface freshwater flux is greatest. The observed changes are consistent with vertical mixing of sea ice meltwater into the upper ocean. The PWP model was developed and run to test

this assertion by seeing if the changes in upper-ocean temperature as well as salinity structure could be simulated by a 1D mixing model driven by realistic surface mechanical and thermal forcing. The conclusion is a qualified yes; PWP simulations produce salinity and temperature changes that account for about 90% of the observed month-to-month changes in the Beaufort Sea SIZ.

The success of the 1D PWP simulations in the Beaufort Sea indicates that the alignment of the freshening pattern with the ice edge position is because salt distribution is almost totally dependent on the amount of local sea ice melt. As a consequence of complete ice melt south of the sea ice edge, the meltwater left behind as

TABLE 2. The ratio 1 **2** [var(DS_{observed} **2** DS_{PWP})/var(DS_{observed})], which describes the fraction of variance in SIZRS-observed monthly salinity change that is accounted for by the PWP. Shown are values for two different depth ranges (0–40 and 0–50 m, chosen because of typical winter mixed layer depth ranges) for each latitude at which the model was run on 1508W.

		728N	748N	768N
Upper 40 m	2012–13	0.9911	0.9502	0.9367
	2013-14	0.9996	0.9960	0.9994
Upper 50 m	2012-13	0.9868	0.9486	0.8430
	2013-14	0.9607	0.9750	0.6746

the edge retreats remains at roughly the same radial position instead of being gathered to the center of the gyre. On an interseasonal time scale, from fall to spring, lateral advection of freshwater in the gyre interior is also small relative to surface vertical fluxes. Observed bulk changes in ice and ocean properties, PWP simulations, and estimates of Ekman convergence suggest 1D mixing of ice meltwater is responsible for about 77%–89% of the upper-ocean salinity changes in this region.

This surface behavior overlies long-term changes in the structure of the Beaufort Gyre, both in its intensification and in its response to the AO. In the past, freshening of the gyre has been associated with con-Ekman transport of fresh surface water (Proshutinsky et al. 2002; Proshutinsky et al. 2009; Giles et al. 2012). These authors and others attribute freshening of the Beaufort Sea to increased anticyclonic wind-driven spinup of the Beaufort Gyre. However, Zhang et al. (2016) show that the Beaufort Gyre has stabilized at a high level since 2008, a timeframe that encompasses our 2012-14 SIZRS campaigns. Similarly, McPhee (2013) indicates that after 2008, ocean geostrophic surface currents were moving at speeds comparable to those of the overlying ice. This stabilization is consistent with our results. In summer and fall of 2012–14, Ekman convergence appears to have a small influence, and the seasonal evolution of freshwater distribution is controlled by 1D mixing processes.

Furthermore, the apparent relationship between Beaufort Gyre strength and hemispheric atmospheric forcing in 2012-14 is not what we had expected. The classical assumption is that because gyre spinup and freshwater content increases occur under anticyclonic forcing of the Beaufort high, the cyclonic influence of a positive AO (Rigor et al. 2002) would cause gyre weakening and a decrease in freshwater content (Proshutinsky et al. 2002). However, Morison et al. (2012) have argued that the Canada Basin freshens under a high AO state because of advection of Eurasian runoff into halocline of the western Arctic Ocean. Our SIZRS 2012-14 results make an even stronger connection. These results associate increased AO with increased doming of the Beaufort Gyre. We have shown that, in addition to bottom pressure and isopycnal tilt, on subannual time scales the AO index acts as a workable proxy for gyre strength when an appropriate lag between atmospheric forcing and oceanic action is considered.

We find that in 2012–14 the seasonal behavior of the surface ocean in the Beaufort Sea SIZ area is dominated by vertical processes as the sea ice cover recedes. It is clear from our SIZRS observations that the seasonal sea ice edge plays a significant and similar role in setting surface ocean properties at the SIZ scale, independent

of how far north this edge lies. Through a modeling investigation, we argue that observed surface freshening in this area may be described as a primarily vertical process, dominating advective influence in the upper 20 m of the study region. The reduced influence of the advective effects may be because by 2012 the ocean had spun up to the point where average surface geostrophic velocities are roughly equal to average sea ice velocities (McPhee 2013). As a consequence, surface stress decreases in magnitude and potentially reverses direction, and the typical average Ekman convergence is small. However, in this semiequilibrated state, a small increase in the AO at monthly time scales resulting in strengthened northeastward wind stress on the northwest part of the Beaufort Sea not sampled by our SIZRS surveys may cause enough Ekman pumping of near-surface water toward the center of the Beaufort Gyre to increase its intensity.

Acknowledgments. Support for this work was provided by Office of Naval Research Grants N00014-12-1-0236 and N00014-12-1-0112. The authors thank Roger Andersen of the University of Washington Polar Science Center for his integral contributions to data collection and processing as well as the men and women of U.S. Coast Guard Air Station Kodiak, without whom SIZRS missions would not have been possible. We also thank Dr. Ilker Fer and two anonymous reviewers, whose suggestions for improving this manuscript were invaluable.

REFERENCES

Aagaard, K., and E. C. Carmack, 1989: The role of sea ice and other fresh water in the Arctic, circulation. J. Geophys. Res., 94, 14485–14498, doi:10.1029/JC094iC10p14485.

Boyer, T. P., O. K. Baranova, M. Biddle, D. R. Johnson, A. V. Mishonov, C. Paver, D. Seidov, and M. Zweng, 2012; Arctic Regional Climatology, Regional Climatology Team, NOAA/NODC. Accessed 18 November 2013. [Available online at www.nodc.noaa.gov/OC5/regional climate/arctic.]

Carmack, E., F. McLaughlin, M. Yamamoto-Kawai, M. Itoh, K. Shimada, and R. Krishfield, 2008: Freshwater storage in the Northern Ocean and the special role of the Beaufort Gyre. Arctic–Subarctic Ocean Fluxes, R. R. Dickson, J. Meincke, and P. B. Rhines, Eds., Springer, 145–169, doi:10.1007/ 978-1-4020-6774-7 8.

Childers, V. A., and J. M. Brozena, 2005: Long-range aircraft as an Arctic oceanographic platform. Deep-Sea Res. I, 52, 2366–2375, doi:10.1016/j.dsr.2005.07.004.

Comiso, J. C., C. L. Parkinson, R. Gersten, and L. Stock, 2008: Accelerated decline in the Arctic sea ice cover. Geophys. Res. Lett., 35, L01703, doi:10.1029/2007GL031972.

Drobot, S., J. Stroeve, J. Maslanik, W. Emery, C. Fowler, and J. Kay, 2008: Evolution of the 2007–2008 Arctic sea ice cover and prospects for a new record in 2008. Geophys. Res. Lett., 35, L19501, doi:10.1029/2008GL035316.

Efron, B., 1979: Bootstrap methods: Another look at jackknife. Ann. Stat., 7, 1–26, doi:10.1214/aos/1176344552.

- Fer, I., A. K. Peterson, A. Randelhoff, and A. Meyer, 2017: One-dimensional evolution of the upper water column in the Atlantic sector of the Arctic Ocean in winter. J. Geophys. Res. Oceans, 122, 1665–1682, doi:10.1002/2016JC012431.
- Giles, K. A., S. W. Laxon, A. L. Ridout, D. J. Wingham, and S. Bacon, 2012: Western Arctic Ocean freshwater storage increased by wind-driven spin-up of the Beaufort Gyre. Nat. Geosci., 5, 194–197, doi:10.1038/ngeo1379.
- Guthrie, J. D., J. H. Morison, and I. Fer, 2013: Revisiting internal waves and mixing in the Arctic Ocean. J. Geophys. Res. Oceans, 118, 3966–3977, doi:10.1002/jgrc.20294.
- Hayes, D. R., and J. H. Morison, 2008: Ice-ocean turbulent exchange in the Arctic summer measured by an autonomous underwater vehicle. Limnol. Oceanogr., 53, 2287–2308, doi:10.4319/lo.2008.53.5 part 2.2287.
- Hibler, W. D., III, 1979: A dynamic thermodynamic sea ice model. J. Phys. Oceanogr., 9, 815–846, doi:10.1175/ 1520-0485(1979)009, 0815:ADTSIM 2.0.CO;2.
- Hyatt, J., 2006: Wind, sea ice, inertial oscillations and upper ocean mixing in Marguerite Bay, western Antarctic Peninsula: Observations and modeling. Ph.D. thesis, Joint Program in Oceanography/Applied Ocean Science and Engineering, Massachusetts Institute of Technology and Woods Hole Oceanographic Institution, 168 pp.
- Jackson, J. M., E. C. Carmack, F. A. McLaughlin, S. E. Allen, and R. G. Ingram, 2010: Identification, characterization, and change of the near-surface temperature maximum in the Canada Basin, 1993–2008. J. Geophys. Res., 115, C05021, doi:10.1029/2009JC005265.
- Jerlov, N. G., 1976: Marine Optics. Elsevier, 230 pp.
- Johnson, G. C., S. Schmidtko, and J. M. Lyman, 2012: Relative contributions of temperature and salinity to seasonal mixed layer density changes and horizontal density gradients. J. Geophys. Res., 117, C04015, doi:10.1029/2011JC007651.
- Kalnay, E., and Coauthors, 1996: The NCEP/NCAR 40-Year Reanalysis Project. Bull. Amer. Meteor. Soc., 77, 437–471, doi:10.1175/1520-0477(1996)077, 0437:TNYRP 2.0.CO;2.
- Lindsay, R., and A. Schweiger, 2015: Arctic sea ice thickness loss determined using subsurface, aircraft, and satellite observations. Cryosphere, 9, 269–283, doi:10.5194/tc-9-269-2015.
- —, M. Wensnahan, A. Schweiger, and J. Zhang, 2014: Evaluation of seven different atmospheric reanalysis products in the Arctic.
- J. Climate, 27, 2588–2606, doi:10.1175/JCLI-D-13-00014.1. Martin, T., M. Steele, and J. Zhang, 2014: Seasonality and long-term trend of Arctic Ocean surface stress in a model. J. Geophys. Res. Oceans, 119, 1723–1738, doi:10.1002/2013JC009425.
- Maslanik, J., J. Stroeve, C. Fowler, and W. Emery, 2011: Distribution and trends in Arctic sea ice age through spring 2011. Geophys. Res. Lett., 38, L13502, doi:10.1029/2011GL047735.
- Maykut, G. A., and M. G. McPhee, 1995: Solar heating of the Arctic mixed layer. J. Geophys. Res., 100, 24 691–24 703, doi:10.1029/ 95JC02554.
- McPhee, M. G., 2008: Air-Ice-Ocean Interaction: Turbulent Ocean Boundary Layer Exchange Processes. Springer, 215 pp.
- ——, 2013: Intensification of geostrophic currents in the Canada Basin, Arctic Ocean. J. Climate, 26, 3130–3138, doi:10.1175/ JCLI-D-12-00289.1.
- ——, A. Proshutinsky, J. H. Morison, M. Steele, and M. B. Alkire, 2009: Rapid change in freshwater content of the Arctic Ocean. Geophys. Res. Lett., 36, L10602, doi:10.1029/ 2009GL037525.
- Morison, J., R. Kwok, C. Peralta-Ferriz, M. Alkire, I. Rigor, R. Andersen, and M. Steele, 2012: Changing Arctic Ocean

- freshwater pathways. Nature, 481, 66–70, doi:10.1038/nature10705.
- Nguyen, A. T., D. Menemenlis, and R. Kwok, 2009: Improved modeling of the Arctic halocline with a subgrid-scale brine rejection parameterization. J. Geophys. Res., 114, C11014, doi:10.1029/2008JC005121.
- Pawlowicz, R., B. Beardsley, and S. Lentz, 2002: Classical tidal harmonic analysis including error estimates in MATLAB using T_TIDE. Comput. Geosci., 28, 929–937, doi:10.1016/S0098-3004(02)00013-4.
- Peralta-Ferriz, C., and R. A. Woodgate, 2015: Seasonal and interannual variability of pan-Arctic surface mixed layer properties from 1979 to 2012 from hydrographic data, and the dominance of stratification for multiyear mixed layer depth shoaling. Prog. Oceanogr., 134, 19–53, doi:10.1016/j.pocean.2014.12.005.
- Perovich, D. K., and Coauthors, 2011: Arctic sea-ice melt in 2008 and the role of solar heating. Ann. Glaciol., 52, 355–359, doi:10.3189/172756411795931714.
- Price, J. F., R. A. Weller, and R. Pinkel, 1986: Diurnal cycling: Observations and models of the upper ocean response to diurnal heating, cooling, and wind mixing. J. Geophys. Res., 91, 8411–8427, doi:10.1029/JC091iC07p08411.
- Proshutinsky, A., R. H. Bourke, and F. A. McLaughlin, 2002: The role of the Beaufort Gyre in Arctic climate variability: Seasonal to decadal climate scales. Geophys. Res. Lett., 29, 2100, doi:10.1029/2002GL015847.
- —, and Coauthors, 2009: Beaufort Gyre freshwater reservoir: State and variability from observations. J. Geophys. Res., 114, C00A10, doi:10.1029/2008JC005104.
- Rabe, B., and Coauthors, 2014: Arctic Ocean Basin liquid freshwater storage trend 1992–2012. Geophys. Res. Lett., 41, 961–968, doi:10.1002/2013GL058121.
- Rigor, I. G., J. M. Wallace, and R. L. Colony, 2002: Response of sea ice to the Arctic Oscillation. J. Climate, 15, 2648–2663, doi:10.1175/1520-0442(2002)015, 2648:ROSITT = 2.0.CO;2.
- Rösel, A., and L. Kaleschke, 2012: Influence of melt ponds on microwave sensors' sea ice concentration retrieval algorithms. Proc. IEEE Int. Geoscience and Remote Sensing Symp. (IGARSS), Munich, Germany, Institute of Electrical and Electronics Engineers, 3261–3264, doi:10.1109/IGARSS.2012.6350608.
- Seidov, D., and Coauthors, 2015: Oceanography north of 608N from World Ocean database. Prog. Oceanogr., 132, 153–173, doi:10.1016/j.pocean.2014.02.003.
- Shimada, K., T. Kamoshida, M. Itoh, S. Nishino, E. Carmack, F. A. McLaughlin, S. Zimmermann, and A. Proshutinsky, 2006: Pacific Ocean inflow: Influence on catastrophic reduction of sea ice cover in the Arctic Ocean. Geophys. Res. Lett., 33, L08605, doi:10.1029/2005GL025624.
- Steele, M., R. Morley, and W. Ermold, 2001: PHC: A global ocean hydrography with a high-quality Arctic Ocean. J. Climate, 14, 2079–2087, doi:10.1175/1520-0442(2001)014, 2079: PAGOHW 2.0.CO:2.
- —, J. Morison, W. Ermold, I. Rigor, M. Ortmeyer, and K. Shimada, 2004: Circulation of summer Pacific halocline water in the Arctic Ocean. J. Geophys. Res., 109, C02027, doi:10.1029/2003JC002009.
- —, J. Zhang, and W. Ermold, 2010: Mechanisms of summertime upper Arctic Ocean warming and the effect on sea ice melt. J. Geophys. Res., 115, C11004, doi:10.1029/2009JC005849.
- —, —, and —, 2011: Modeling the formation and fate of the near-surface temperature maximum in the Canadian Basin of the Arctic Ocean. J. Geophys. Res., 116, C11015, doi:10.1029/ 2010JC006803.

- Thompson, D. W. J., and J. M. Wallace, 1998: The Arctic Oscillation signature in the wintertime geopotential height and temperature fields. Geophys. Res. Lett., 25, 1297–1300, doi:10.1029/ 98GL00950.
- Timokhov, L., and F. Tanis, Eds., 1997: Environmental Working Group Joint U.S.-Russian Atlas of the Arctic Ocean, version 1. National Snow and Ice Data Center, CD-ROM, doi:10.7265/ N5H12ZX4.
- Toole, J. M., M.-L. Timmermans, D. K. Perovich, R. A. Krishfield, A. Proshutinsky, and J. A. Richter-Menge, 2010: Influences of the ocean surface mixed layer and thermohaline stratification on Arctic Sea ice in the central Canada Basin. J. Geophys. Res., 115, C10018, doi:10.1029/2009JC005660.
- Untersteiner, N., 1988: On the ice and heat balance in Fram Strait.

 J. Geophys. Res., 93, 527–531, doi:10.1029/JC093iC01p00527.
- Vinogradova, N. T., R. M. Ponte, and D. Stammer, 2007: Relation between sea level and bottom pressure and the vertical de-

- pendence of oceanic variability. Geophys. Res. Lett., 34, L03608, doi:10.1029/2006GL028588.
- Woodgate, R. A., K. Aagaard, and T. J. Weingartner, 2006: Interannual changes in the Bering Strait fluxes of volume, heat and freshwater between 1991 and 2004. Geophys. Res. Lett., 33, L15609, doi:10.1029/2006GL026931.
- Zhang, J., R. Lindsay, M. Steele, and A. Schweiger, 2008a: What drove the dramatic retreat of Arctic sea ice during summer 2007? Geophys. Res. Lett., 35, L11505, doi:10.1029/ 2008GL034005.
- —, M. Steele, R. Lindsay, A. Schweiger, and J. Morison, 2008b: Ensemble 1-year predictions of Arctic sea ice for the spring and summer of 2008. Geophys. Res. Lett., 35, L08502, doi:10.1029/2008GL033244.
- —, and Coauthors, 2016: The Beaufort Gyre intensification and stabilization: A model-observation synthesis. J. Geophys. Res. Oceans, 121, 7933–7952, doi:10.1002/2016JC012196.